https://doi.org/10.5194/egusphere-2023-1570
Preprint. Discussion started: 2 August 2023

Observability of Moisture Transport Divergence in Arctic Atmospheric Rivers by Dropsondes

Henning Dorff[1,2], Heike Konow[3,1], Vera Schemann[4], and Felix Ament[1,3]

[1]University of Hamburg, Hamburg, Germany
[2]International Max Planck Research School on Earth System Modelling, Max Planck Institute for Meteorology, Hamburg, Germany
[3]Max Planck Institute for Meteorology, Hamburg, Germany
[4]University of Cologne, Cologne, Germany

Correspondence: henning.dorff@uni-hamburg.de

Abstract. This study emulates dropsondes to elucidate how adequately sporadic airborne sondes represent divergence (convergence) of moisture transport in arctic Atmospheric Rivers (ARs). The convergence of vertically integrated moisture transport (IVT) plays a crucial role as it favours precipitation that significantly affects arctic sea ice properties. Long range research aircraft can transect ARs and dropsondes determine their IVT divergence. However, a limited number of sondes may deteriorate the representation of IVT variability and divergence. We disentangle errors arising from undersampling by discrete soundings and from the flight duration in order to assess the representativeness of future sonde-based IVT divergence in arctic ARs.

Our synthetic study uses CARRA reanalyses to set up an idealised scenario for airborne AR observations. For nine arctic spring ARs, we mimic flights transecting each AR in CARRA and emulate sonde-based IVT representation by picking single vertical profiles. The emulation quantifies IVT divergence observability by two approaches. First, sonde-based IVT and its divergence are compared to the continuous IVT interpolated onto the flight cross-section. The comparison specifies uncertainties of discrete sonde-based IVT variability and divergence. Second, we determine how temporal AR evolution affects IVT divergence values by contrasting time-propagating sonde-based values with the divergence based on instantaneous snapshots.

For our arctic AR cross-sections, we find that moisture transport variability contributes less than 10 % to its lateral mean, while wind and moisture variability individually are higher. Both quantities can be uncorrelated and do not consistently exhibit a coherent pattern. Moisture turns out as the more varying quantity. We show that sounding spacing greater than 100 km results in errors greater than 10 % of the total IVT along AR cross-sections. For IVT divergence, the arctic ARs exhibit similar gradients in moisture advection and mass convergence across the embedded front as mid-latitude ARs, but we identify moisture advection being dominant. We overall confirm their observability with an uncertainty lower than 25 % by a sequence of at least seven sondes per cross-section. Rather than sonde undersampling, it is the temporal AR evolution over the flight duration that leads to higher deviations in divergence components. Dedicated planning of sonde-based IVT divergence purposes should not only involve sonde positioning but rather pursue optimizing the flight duration. Our benchmarks quantify sonde-based uncertainties as a prerequisite to be used for future airborne moisture budget closure in arctic ARs.

https://doi.org/10.5194/egusphere-2023-1570
Preprint. Discussion started: 2 August 2023

1 Introduction

Narrow water vapour rich corridors, Atmospheric Rivers (ARs), occassionally flood the Arctic. In the polar regions, they account for 70 % of poleward moisture transport (Nash et al., 2018) with significant impacts (Gorodetskaya et al., 2014; Neff, 2018). Along the pathways of ARs, the moist and warm air masses undergo transformations that imply phase transitions, surface interaction or trigger significant precipitation (Lavers et al., 2016; Vázquez et al., 2018; You et al., 2022). The impacts range up to significant warming causing sea- and Greenland ice retreat (Gimeno et al., 2014; Woods and Caballero, 2016; Mattingly et al., 2018). To illuminate moisture transformation processes and surface interactions (e.g. Papritz et al., 2021; You et al., 2022) occuring in arctic ARs, we have to analyse the characteristics of the moisture transport, i.e. the vertical Integrated Water Vapour Transport (IVT). The moisture budget links the evolution of ARs and their precipitation efficiency by the divergence of IVT (Seager and Henderson, 2013).

While the IVT variability and the contribution of IVT divergence to the moisture budget are widely assessed over the mid latitudes (e.g. Guan et al., 2020; Tan et al., 2021), we lack an understanding of their magnitudes explicitly in the Arctic. Reanalysis data have been established a manifold understanding of global IVT variability in ARs (e.g. Guan and Waliser, 2015). Yet, such studies mostly stem of coarser grid reanalyses such as ERA-Interim and MERRA-2 (e.g. Guan and Waliser, 2017). Only recent studies include higher resolution reanalyses such as ERA5 which achieve more accurate AR-IVT representation (Cobb et al., 2021b). High-resolution observations so far mainly exists for mid-latitude events that exhibit more intense moisture transport (e.g Norris et al., 2020; Cobb et al., 2022) but, in turn, lack for the Arctic.

Still, the observation of arctic AR-IVT is challenging. One reason is the remote and sporadic occurence of arctic ARs over the ocean basins. Moreover, the quantification of AR moisture budget components, such as the divergence of moisture transport, requires sufficiently large horizontal corridors to be observed. ARs generally exhibit strong moisture transport gradients along their cross-section (e.g. Ralph et al., 2017; Demirdjian et al., 2020). Since ARs mainly occur in conjuction with a cold front, different dynamical and thermodynamical processes act on the moisture transport and its divergence along the frontal cross-section (Guan et al., 2020, Cobb et al., 2021a). Other than that, moisture transport observation has to rely on simultaneous measurements of winds and moisture. Dropsondes can measure the vertical profiles of both quantities and thus the moisture transport so that they close a data gap remaining from remote sensing and from spaceborne or ground-based observations in general (Zheng et al., 2021). From long-range research aircraft, sonde releases enable the observation of IVT divergence in extended sectors of ARs. First airborne studies determine IVT divergence in mid-latitude ARs (e.g. Norris et al., 2020) and begin complementing large reanalysis-based statistics of AR moisture budget components (Guan et al., 2020).

However, a limited number of dropsondes may deteriorate the IVT representation and consequently the divergence values. Accordingly, studies assess the impact of sounding frequency on AR-IVT variability (e.g. Ralph et al., 2017; Guan et al., 2018), but so far purely for mid-latitude ARs. Besides sonde-based undersampling, we hypothesize that the AR evolution over the flight duration enclosing the AR corridor can also affect the results non-negligibly. Before sondes infer the actual IVT divergence in arctic ARs, we disentangle sonde-based errors that arise from undersampling by discrete sounding and from non-instantaneous sampling over the flight duration. Therefore, we examine how moisture transport variability is composed in

https://doi.org/10.5194/egusphere-2023-1570
Preprint. Discussion started: 2 August 2023

arctic ARs close to the sea ice (i.e. Fram Strait and Greenland Sea). Our study monitors AR moisture transport as seen from long-range research aircraft to tackle how such aircraft infer arctic AR moisture transport variability by adressing the questions:

- (Q1) What is the maximum distance between sondes to determine the total moisture transport through AR corridors?
- (Q2) How correlated are moisture and winds in arctic ARs and do coherent patterns contribute significantly to IVT?

As a prerequisite to close the moisture budget for arctic AR cross-sections, we assess the observability of moisture transport (IVT) divergence by dropsondes and quantify uncertainties in its representativeness. Our divergence assessment comprises:

- (Q3) How does divergence of moisture transport characterise along the cross-section of arctic ARs?
- (Q4) To what extent can discrete and non-instantaneous sondes reproduce IVT divergence in the light of the AR evolution during flight?

To pursue Q1-Q4, we look at arctic ARs, that we pre-identified in ERA5 and investigate them within the novel C3S Arctic Regional Reanalysis (CARRA). The high spatial resolution of CARRA illuminates kilometer-scale moisture transport variability inside arctic ARs and forms our idealized background reality. In CARRA, we consider nine arctic AR events along synthetic flights transecting and enclosing an AR corridor. We emulate synthetic dropsondes along the tracks by depicting single vertical profiles. Our study compares actual IVT variability and divergence along the tracks with the emulated sonde-based IVT representation. This synthetic comparison estimates the observability of arctic AR-IVT divergence from sondes.
Section 2 presents our considered AR events in CARRA. Section 3 describes the methods emulating dedicated flight pattern and the synthetic soundings, and how we derive moisture transport divergence. For this framework, Section 4 deals with the IVT variability. This entails total moisture transport in arctic ARs and their IVT variability along cross-sections, their sonde-based representation (Q1) and the coherence of moisture and winds (Q2). Section 5 specifies the moisture transport divergence (Q3) and compares its continuous representation to that by synthetic sondes. Section 6 quantifies airborne deviations arising from AR evolution over flight duration which is mostly idealized as stationary (Q4). Our assessment provides benchmarks of uncertainties in the sonde-based IVT divergence for arctic AR and facilitates flight mission planning.

2 Arctic AR moisture transport data

2.1 Dropsondes on long-range research aircraft

This study relies on the flight performance of state-of-the-art long-range research aircraft. We exemplarily refer to the High Altitude and LOng Range Research Aircraft (HALO), equipped with a remote sensing configuration described in more detail in Stevens et al. (2019) and Konow et al. (2021). A similar aircraft examines pacific ARs (Cobb et al., 2022). Both aircraft allow along-track observations during flight at common cruising levels above 10 km and a ground speed of around 250 m/s.
Such aircraft release GPS-dropsondes. During their fall, the sondes take various measurements, e.g. relative humidity and wind speed with an accuracy of 1 % and 0.1 m/s, respectively (George et al., 2021; Konow et al., 2021). The simultaneous measurements allow to derive the moisture transport and its divergence inside Arctic ARs. We refer to such a sonde principle,

https://doi.org/10.5194/egusphere-2023-1570
Preprint. Discussion started: 2 August 2023

Table 1. Specifications of used reanalyses for AR analysis

Reanalysis Dataset	Horizontal Resolution	Vertical resolution up to 10 km (250 hPa)	Time resolution
ERA5	0.25 x 0.25 deg	21 levels	hourly
CARRA	2.5 x 2.5 km	15 levels	(forecast hourly)

but we neglect the explicit measurement uncertainties for both quantities. Instead, we target the overall representativeness of airborne sonde-based IVT. For arctic conditions, we synthetically assess sonde-based uncertainties in lateral moisture transport variability, its maximum intensity and position and how the uncertainties affect airborne IVT divergence calculations.

2.2 Reanalysis data

This observability study relies on a reanalysis framework (Tab. 1). The ECMWF Reanalysis v5 (ERA5) (Hersbach et al., 2020) identifies our ARs of interest. Against other global reanalyses, ERA5 outperforms AR characteristics (Graham et al., 2019; Cobb et al., 2021b). Recent studies consider ERA5 to investigate AR conditions explicitly in the Arctic (Fearon et al., 2021; Zhang et al., 2022). At the Fram Strait and Greenland Sea, the lat-lon grid from ERA5 yields approximately 30 km distances. For the flight performance (Sect. 2.1), sounding resolutions of 30 km require releases every 2 minutes. This is higher than commonly conducted sounding frequencies. However, to cover undersampled variability between the sondes even better, we include the C3S Arctic Regional Reanalysis (CARRA), accessible by Schyberg et al. (2021), having a 2.5 km horizontal resolution. Driven by lateral boundary conditions from ERA5, CARRA includes more observations and hourly forecasts by the HARMONIE-AROME model (Bengtsson et al., 2017). Køltzow et al. (2022) verified the improved representation in arctic surface-near meteorological conditions. Both pressure-level reanalyses are provided by the Copernicus Climate Data Store (CDS).

2.3 Selected Atmospheric River cases

Our study comprises ARs from nine spring days between 2011 and 2020. Figure 1 presents these ARs extending over the North Atlantic and Arctic Ocean. Accordingly, we are interested in ARs causing airmasses to overshoot the sea ice edge in the Arctic ocean. As a valid AR detector we use IVT that represents AR strength as:

$$IVT = -\frac{1}{g} \cdot \int_{p_{\mathrm{sfc}}}^{p_{\mathrm{top}}} q\mathbf{V}\, dp \tag{1}$$

where $\mathbf{V}$ is the horizontal wind vector and q the specific humidity. We use IVT-based AR detection by Guan (2022) to select our arctic ARs from spring season. The selected ARs take typical arctic pathways (Fig. 1). Usually, arctic ARs evolve on the eastern flank of low-pressure systems forcing large-scale meridional transport representing a common synoptic composition (Papritz and Dunn-Sigouin, 2020). Blocking situations can favor even more meridional circulation. Some of the ARs exhibit

https://doi.org/10.5194/egusphere-2023-1570
Preprint. Discussion started: 2 August 2023

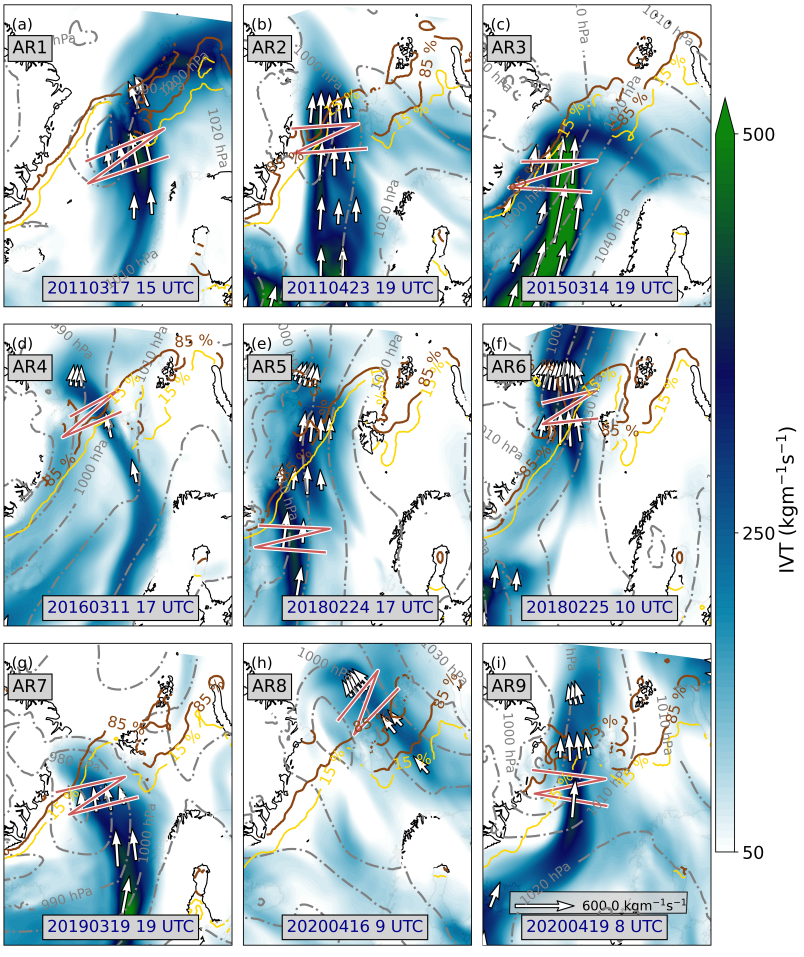

Figure 1. IVT contours of investigated AR events from ERA5. Red lines represent the zig-zag flight pattern to investigate the moisture budget in AR corridors. Grey lines indicate surface isobars, while brown (orange) contour lines specify sea ice cover thresholds given in %. The arrows depict the magnitude and orientation of IVT. Background maps were made with Natural Earth.

straight meridional moisture transport north of Iceland and approach or exceed Svalbard (AR1, AR2, AR3). AR4 and AR7 show more elongated filaments along the Norwegian coast but still reach far north. We select eight independent events wherein AR5 is also considered for the consecutive day (AR6). At this stage, the centre of AR6 reaches close to the North Pole. Another event originates from Siberia (AR8) that represents another significant roadway for arctic moisture intrusions (Komatsu et al., 2018). The last events in 2020 (AR8, AR9) are accompanied by a warm air intrusion period observed by the Multidisciplinary drifting Observatory for the Study of Arctic Climate (MOSAiC) expedition (Shupe et al., 2022), studied in Kirbus et al. (2023).

Since our analysis is restricted to a small set of ARs, we put them into perspective of spring climatology. Picking the events from the AR catalogue of Guan (2022), Figure 2 compares the latitude of their AR centres and mean IVT with the long-term distribution (1979–2019) for spring ARs along the Atlantic pathway. The distribution indicates that ARs centred further north

https://doi.org/10.5194/egusphere-2023-1570
Preprint. Discussion started: 2 August 2023

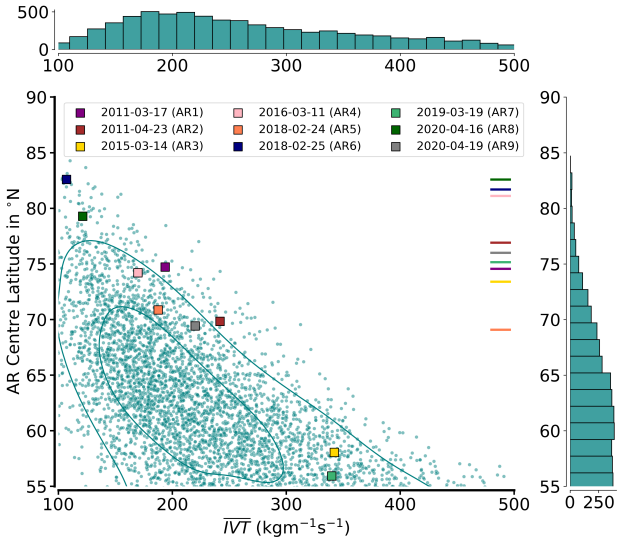

Figure 2. Comparison of selected AR events to long-term statistics (1979–2019) regarding mean IVT and AR centre latitude at given reanalysis time step (ERA-Interim) based on the AR catalogue (Guan, 2022). Isolines represent 25 and 75 percentiles of the kernel density estimate. Coloured lines on the right indicate the centre of the respective flight pattern.

are aligned with less intense mean IVT. Our selected ARs characterise a higher intensity compared to the long-term mean. Most events are centred above 65°N with mean IVT below $300\,\mathrm{kg\,m^{-1}\,s^{-1}}$ which is also not exceeded in the climatology. AR3 and AR7 are centred below 60°N, aligned with mean IVT values around $350\,\mathrm{kg\,m^{-1}s^{-1}}$. Despite their southern centre, they reach far north with $IVT > 250\,\mathrm{kg\,m^{-1}s^{-1}}$ inside the Fram Strait (Fig. 1), so that we declare them as arctic ARs. The flights transecting AR corridors are located in vicinity of the arctic sea ice edge and mainly north of the AR centre (Fig. 2).

3 Airborne strategy for AR moisture transport divergence

The moisture transport divergence is one key component contributing to the overall atmospheric moisture budget. In a vertically integrated perspective, the moisture budget components consist of:

$$\underbrace{\frac{\delta IWV}{\delta t}}_{\text{local change in Integrated Water Vapour}} = \underbrace{E}_{\text{Evaporation}} - \underbrace{P}_{\text{Precipitation}} - \underbrace{\nabla IVT}_{\text{Divergence of Integrated Water Vapour Transport}}, \tag{2}$$

with all components in kilogram per metre squared per second. Seager and Henderson (2013) include another term in Eq. 2, being the moisture flux through a tilted bottom pressure surface, but this is less relevant here. Precipitation and evaporation refer to surface values, while the integrated water vapour IWV and integrated water vapour transport IVT (Eq. 1) represent the vertically integrated quantities. We calculate CARRA-IVT as the trapezoidal integral along the pressure levels (Tab. 1). The following section specifies our airborne strategy to derive ∇IVT in arctic ARs therefrom and the sonde emulation.

https://doi.org/10.5194/egusphere-2023-1570
Preprint. Discussion started: 2 August 2023

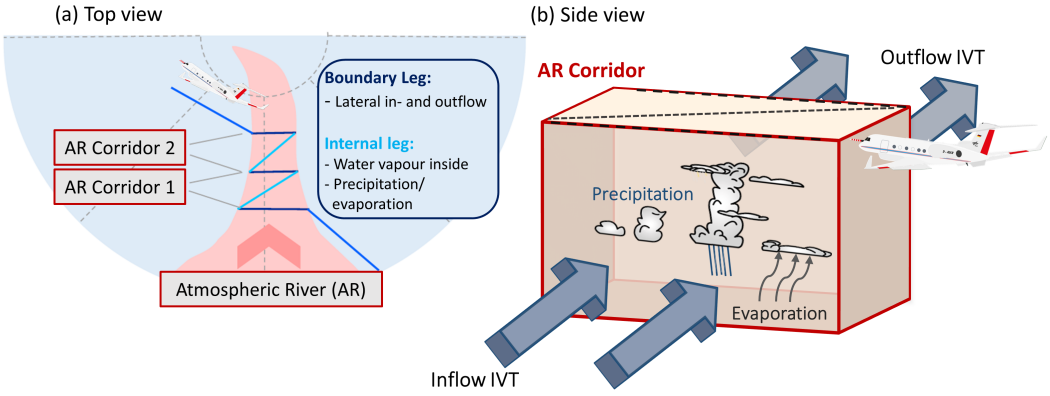

Figure 3. Top (a) and side (b) view on envisioned zig-zag flight pattern to derive the moisture budget components inside AR corridors.

3.1 Flight pattern and emulating observations

The main perspective is the airborne observability of ∇IVT inside arctic ARs. To mimic real observations as a prerequisite for upcoming campaigns, this section emulates sophisticated flight patterns and creates synthetic soundings along the flights.

3.1.1 Zig-zag flight tracks observing AR corridors

The airborne derivation of moisture transport divergence requires sophisticated flight patterns well sampling a specific AR corridor. In general, tracks enclosing corridors, e.g. circles, allow divergence calculations best and are frequently applied for closure purposes (Bony and Stevens, 2019). However, ARs exhibit cross-frontal inhomogenities (Cobb et al., 2022) that smooth out in single circles. The high lateral variability in AR transport characteristics requires stacked or zig-zag patterns with long legs crossing the AR front to capture the heterogenity more sufficiently. Figure 3 sketches how the latter pattern is conceptionally applied in order to close the moisture budget in ARs. The zig-zag pattern observes AR corridors, i.e. box sections along its transport direction. Diagonal internal legs assess precipitation rate, evaporation or water load inside. The boundary legs perpendicular to the major flow quantify the corridor in- and outflow, i.e. in- and outgoing IVT for the entire lateral AR extension. These legs enable simplified divergence calculations. We select AR corridors at the sea ice edge to place the zig-zag flight pattern in (Fig. 1). The corridor boundary legs orientate orthogonally to the major IVT direction. The zig-zag patterns extend in such a way that they cover entire AR cross-sections, meaning the prefrontal warm sector, the AR core with highest IVT and the postfrontal AR cold sector. We fly over open ocean and sea ice but disregard land. The tracks mimic idealised flight performances. The aircraft location refers to 1 Hz resolution which is a common resolution of remote sensing products, such as the HAMP dataset comprising radiometer and radar (Mech et al., 2014; Konow et al., 2019). We assume a constant ground speed of 250 m s^{-1} but neglect the duration for turns. We choose a constant flight altitude of 10,000 m.

https://doi.org/10.5194/egusphere-2023-1570
Preprint. Discussion started: 2 August 2023

3.1.2 Synthetic observations

Using this idealised performance, the zig-zag patterns (shown in Fig. 1) require roughly 2–3 h to be completed, and up to 1 h for the single AR cross-sections (not shown). Up to three reanalysis timesteps represent atmospheric conditions during our pattern. We upsample the reanalysis datasets to minutely frequency by linear time interpolation. Meteorological values along the flight are chosen from the nearest minute and spatially interpolated using harvesine distances. Although the upsampling leaves the model physics at intermediate timesteps, we declare this as a suitable airborne estimate of atmospheric conditions in dynamic systems like ARs, exhibiting significant spatial displacement.

Along the continuous airborne AR representation, we place synthetic soundings for which we neglect any vertical drift or fall time. We further neglect pure measurement uncertainties. Mimicking such effects is out of the scope of this study although it may be crucial when evaluating real sonde profiles with model data. Instead, our sondes observe exact IVT values at their release position. Accordingly, our assessment focusses on the spatial representativeness of dropsondes and especially how their release frequency may affect the airborne understanding of moisture transport variability and its divergence in arctic ARs.

3.2 Sonde-based divergence derivation

To determine IVT divergence (∇IVT), the Gaussian Theorem sets the moisture flux over the perimeter of a closed surface equal to its divergence. However, our flight pattern has open boundaries at the outer sides. Only if lateral flow can be neglected, we obtain the divergence by subtracting the inflow in the entrance leg from the streamward outflow (Fig. 3). Given this limitation, Lenschow et al. (2007) alternatively suggests the regression method. Under linear variations, a meteorological quantity Φ (e.g. wind speed), being stationary in time, can be inferred as:

$$\Phi = \Phi_o + \frac{\delta\Phi}{\delta x} \cdot \Delta x + \frac{\delta\Phi}{\delta y} \cdot \Delta y, \tag{3}$$

with the area mean value Φ_o and Δx and Δy being zonal, meridional displacements from the area centre point. Using the values of Φ at sounding locations and minimising the least-squared errors in the linear regression fit of Eq. 3, we obtain a linear estimate of zonal (x) and meridional (y) gradients, along with the intercept for the line, providing the mean mesoscale value for Φ. Adding up both gradients, we calculate the divergence. Bony and Stevens (2019) and George et al. (2021) proved the feasibility of this method by comparing its divergence values with the Gaussian-based line integral over flown circles.

Having the mathematical expression, we specify the impact of IVT divergence with respect to the moisture budget. In case of evaporation E being negligible compared to the other terms of Eq. 2 (what approximately holds for the open Arctic Ocean), convergence of integrated moisture transport either causes precipitation or locally increases the amount of water vapour. Since convergence of moisture transport hence has two different impacts, ∇IVT can be split into two composits:

$$\nabla IVT = -\frac{1}{g \cdot \rho_w} \cdot \int_{p_{\mathrm{sfc}}}^{p_{\mathrm{top}}} \nabla\,(q\mathbf{V})\,dp = \underbrace{\frac{1}{g \cdot \rho_w} \cdot \int_{p_{\mathrm{sfc}}}^{p_{\mathrm{top}}} q\,(-\nabla\mathbf{V})\,dp}_{\text{dynamical mass convergence (CONV)}} + \underbrace{\frac{1}{g \cdot \rho_w} \cdot \int_{p_{\mathrm{sfc}}}^{p_{\mathrm{top}}} \mathbf{V}\,(-\nabla q)\,dp}_{\text{integral of horizontal moisture advection (ADV)}} \quad . \tag{4}$$

https://doi.org/10.5194/egusphere-2023-1570
Preprint. Discussion started: 2 August 2023

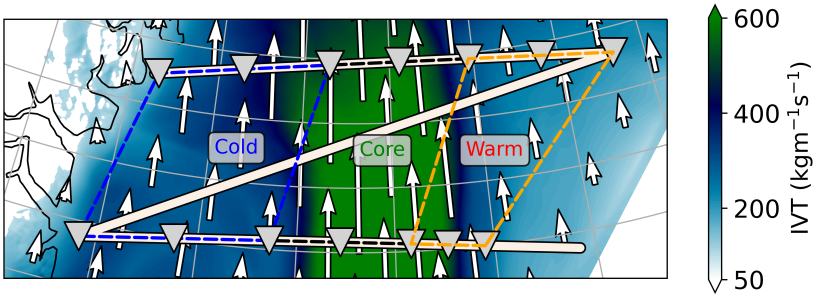

Figure 4. Illustration of AR cross-section sectors and placed sondes in order to calculate the divergence for AR3. IVT contours refer to CARRA at the hour mid of the flight corridor. Background map is made with Natural Earth.

The first term represents the dynamical mass convergence being the product of the moisture mass and divergence. The mass convergence term can be related to vertical velocity via the continuity equation and itself is closely linked to precipitation (Wong et al., 2016; Norris et al., 2020). The second term represents the horizontal advection of moisture that is little correlated to precipitation formation (Guan et al., 2020). To calculate ADV and $CONV$, we use the regression method. Finally, all terms in Eq. 4 are divided by the density of water ρ_w to provide budget contributions in mm per day (mm d^{-1}).

3.3 Decomposition in frontal AR sectors

Current research considering observations along AR cross-sections suggests to distinguish between different sectors across the front the AR is embedded in. This separation results from the AR occurence mostly within the vicinity of cold fronts where distinct processes take place. Using airborne observations of a large set of pacific AR cross-sections, Cobb et al. (2021a) classified different sectors of ARs based on the frontal position and IVT. This comprises a warm sector being pre-frontal, the AR core with highest IVT ($> 80\,\%$ of maximum IVT) and the post-frontal cold sector. Similarly, Guan et al. (2020) refer to their global AR catalogue and separate AR cross-sections for IVT divergence calculations across the major AR axis.

We conduct such sector-based decomposition of IVT divergence for our arctic AR events in CARRA. Figure 4 illustrates the frontal sector decomposition for our most intense AR (AR3). Our decomposition aligns with the requirements given in Cobb et al. (2021a). However, we lower the IVT-threshold defining AR edges from 250 to 100 kg m^{-1} s^{-1}. This fits to common polar moisture transport magnitudes exceeding the 95th percentile used in the AR detection of Guan and Waliser (2015). Otherwise, as statistics in Fig. 2 indicate, we would exclude most ARs north of 70°N, or would shrink the AR cross-section so that most transport is ignored. As shown in Fig. 4, three synthetic sondes calculate the IVT divergence for each sector respectively. We emphasise that our IVT-determined frontal AR sectors along the flight track tilt while the IVT corridor has a straight northward orientation in Fig 4. This putative inconsistency arises from the north-eastward displacement of the AR filament over the course of the 2.5 h synthetic flight section (Sect. 2.1). Accordingly, Sect. 6 examines the extent to which sonde-based IVT divergence is affected by flight duration, as opposed to actually looking at the AR in an instantaneous snapshot.

https://doi.org/10.5194/egusphere-2023-1570
Preprint. Discussion started: 2 August 2023

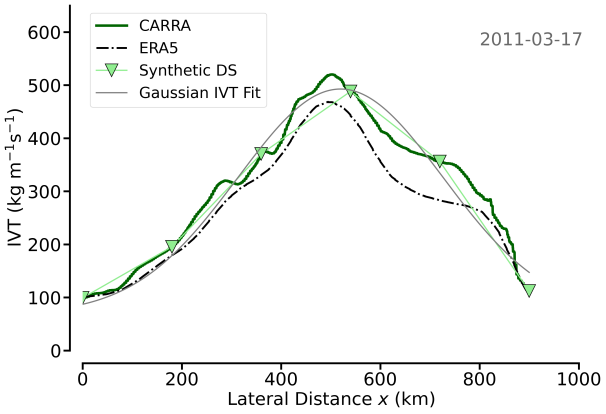

Figure 5. Inflow AR-IVT cross-section from AR1 (2011-03-17) with six synthetic soundings placed along the track. A gaussian fit based on the sounding IVT representation is calculated.

4 Moisture transport in Arctic AR cross-sections and its variability

This section investigates IVT variability within our arctic ARs (Sect. 2.3) using the high-resolution CARRA (Sect. 2.2). First, we analyse the shape of IVT (and document the larger IVT variability compared to forcing ERA5). Next, we focus on the observability of prevailing AR moisture transport variability by discrete soundings, using the synthetic sondes (Sect. 3). We determine the maximum distance between sondes needed to derive the total moisture transport in AR cross-sections accurately (Q1). Finally, we describe how coherence in moisture and wind speed contributes to moisture transport and its variability (Q2).

4.1 Shape of IVT across arctic ARs

As observed in mid-latitudes (Ralph et al., 2017), IVT through AR cross-sections is commonly bell-shaped. Here, we infer whether arctic ARs feature the same structure. For AR1, Figure 5 illustrates the cross-sectoral IVT along the inflow flight leg. We recognise the bell-shaped IVT from both, CARRA and forcing ERA5. Within the cross-section centre which we declare as the AR core (Sect. 3.3), CARRA, however, shows stronger moisture transport with a more pronounced IVT maximum. Moreover, CARRA increases the cross-section variability for this case.

This increased lateral variability of IVT in CARRA arises the question, how sporadic soundings can reproduce such AR-IVT patterns. Using the synthetic soundings (Sect. 3.1.2) which consider CARRA as idealised reality, a set of six equidistant sondes would reveal a slightly different pattern of the AR cross-section in Fig. 5. A gaussian fit using the discrete soundings in a least-square sense can reproduce the bell-shaped distribution of AR-IVT. Yet, the fit is very sensitive to the actual positions of dropsonde releases. While the centred sonde in Fig. 5 is located close to the IVT maximum ($IVT_{\max}$), slight displacements of this release which easily occur in real observations, can rapidly cause an underestimation of the AR core moisture transport. Summarising all cross-sections of our ARs from Sect. 2.3, most arctic AR cross-sections maintain the typical bell-shaped IVT curve over widths of roughly 400–800 km and indicate pronounced IVT maxima in the core of 300–600 kg m^{-1}s^{-1} (not

https://doi.org/10.5194/egusphere-2023-1570
Preprint. Discussion started: 2 August 2023

shown). Only for the weak AR8, this structure is less pronounced. We highlight that maximum (mean) values of IVT per cross-section increase by roughly 9 % (8 %) from ERA5 to CARRA on average. CARRA further increases the IVT variability by roughly 11 %. This is an outcome of the higher horizontal resolution than in ERA5. While sonde positions in Fig. 5 are suitable to represent the cross-section IVT, other ARs signify more complexity in being accurately represented by this number of placed soundings. We need further inspections on how sounding intervals deteriorate the AR moisture transport observability.

4.2 Sonde-based total cross-section moisture transport

The most intuitive approximation of ∇IVT in AR corridors relies on deriving the Total Integrated Water Vapour Transport ($TIVT$) through the boundary legs. Following Ralph et al. (2017), $TIVT$ of a cross-section is defined as:

$$TIVT = \int IVT\, dx, \tag{5}$$

representing the lateral integral of IVT over the flight distance x in one boundary leg (in- or outflow). Assuming that no moisture flux exists apart from perpendicular to the flight track, we can approximate ∇IVT in an AR corridor by the difference of in- minus outgoing $TIVT$ of the cross-sections. To assess the required sounding frequency, we vary the number of synthetic sondes. For AR1, one of the stronger events with $IVT_{\text{max}} \approx 500\,\text{kgm}^{-1}\text{s}^{-1}$ (presented in Fig. 5), we find that the release of six sondes underestimates $TIVT$ by roughly 10 % against the continuous AR-IVT representation in CARRA. In contrast, $TIVT$ estimates based on ten sondes differ by less than 1 % (not shown). When lowering the number of releases, their location becomes more essential and strongly affects the derived moisture transport variability especially in the AR core with possible occurence of a low-level jet (LLJ). This sector accounts for $\approx 50\,\%$ of the entire moisture transport through the cross-section (Guan and Waliser, 2017). Too large sonde distances enhance the probability to miss this IVT dominating region.

Figure 6 illustrates the outcome of a bootstrapping approach wherein we sample the cross-sections with varying release intervals and positions. We apply this method to all arctic ARs (Sect. 2.3). The emerging boxplot (Fig. 6) reveals how many sonde releases are needed to derive $TIVT$ in our chosen ARs cross-sections. Accordingly, the relative error of $TIVT$ against the continuous AR representation starts to significantly increase for sounding intervals above 10 min (distances of 150 km at a cruise speed of 250 ms^{-1} and roughly five sondes for the given cross-section lengths). For intervals above 15 min, sonde-based $TIVT$ can strongly deviate. We find that $TIVT$ uncertainty increases less rapidly with larger sonde intervals than in mid-latitude case studies (Ralph et al., 2017; Guan et al., 2018), but emphasise that our arctic $TIVT$ values extend to roughly one third of the mid-latitude range of $8 - -10 \cdot 10^8\,\text{kg}\,\text{s}^{-1}$. We conclude that a minimum number of five releases must be targeted. The IVT variability that causes such sonde errors in $TIVT$ is strongly correlated to IVT_{max} (correlation coefficient $r = 0.91$). Hence, we expect more sondes to be required for the strongest AR events. However, the coloured boxes in Fig. 6 indicate that the distribution of the relative $TIVT$ error behaves similarly, when we pick cross-sections with IVT_{max} larger than the 75th percentile from the bootstrapping sample (mainly AR1 and AR3). The mean relative error increases more rapidly with larger sounding intervals whereas the spread is lower than for the entire sample. Highest $TIVT$ errors thus do not originate from the strong events when having very few sondes. For larger sounding intervals ($\leq 15\,\text{min}$), the mean error and its spread becomes lower than for the entirety.

https://doi.org/10.5194/egusphere-2023-1570
Preprint. Discussion started: 2 August 2023

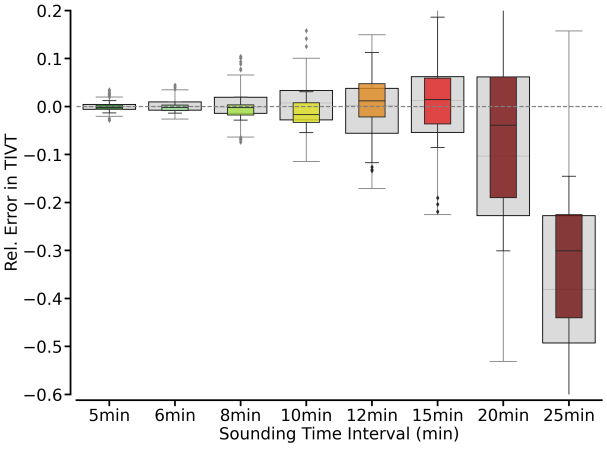

Figure 6. Relative error in $TIVT$ as a function of sounding frequency in seconds for all AR cross-sections (grey) and colored, those including highest IVT maxima (75th percentile). For an assumed aircraft speed of 250 m s^{-1}, 5 min (300 s) sounding spacing results in profile distances of 75 km (if sonde drifts are neglected).

4.3 Variability of moisture and wind in arctic ARs

After investigating the overall moisture transport by its vertical integral IVT, it is intuitive to take a deeper look at vertical moisture q and wind v (Eq. 1) individually, and to compare arctic ARs to what we know from mid-latitude ARs. We examine the cross-section variability of v and q in the vertical using the continuous representation of our arctic ARs (Fig. 7). Moisture transport in the lowest levels up to 850 hPa contributes to IVT with roughly 50 %. Up to this height, both high moisture and wind speeds are predominant. Further upwards, wind speed even accelerates up to $15--30\,\mathrm{m\,s^{-1}}$ and q decreases with height, remaining below $5\,\mathrm{g\,kg^{-1}}$ in arctic ARs. These characteristics resemble soundings of ARs over the North-East Pacific (Cobb et al., 2021b). Still, we find some notable differences to mid-latitude ARs. Whilst low-level wind speed is comparable to that in the Pacific region (Ralph et al., 2004; Cobb et al., 2021a), q is considerably lower. The wind profile behaves more homogeneous in the vertical than registered from sub-tropical/mid-latitude cases (Ralph et al., 2005; Cobb et al.,2021a). Above a slight bump at 900 hPa, mostly designated as LLJ (Ralph et al., 2004; Demirdjian et al., 2020), the wind speed slightly decreases before continues increasing. Since the atmosphere dries with height, the moisture transport declines.

The cross-sectoral variability of both quantities strongly affects IVT variability. Figure 7 exemplarily depicts our most intense AR (AR3). The LLJ in AR3 with high wind speeds above $30\,\mathrm{m\,s^{-1}}$ causes strong moisture transport whereas moisture is more or less average. While strong moisture transport originates from strong winds, its cross-sectoral variability is mostly affected by moisture variability. The strong AR3 suggests that moisture varies strongly and seemingly dominates moisture transport variability in arctic ARs, when winds are overall strong.

Aiming at an identification of the more variable quantity out of q and v can improve measurement strategies. Specifically, moisture can be derived from supplementary remote sensing devices on long-term research aircrafts. For wind and moisture,

https://doi.org/10.5194/egusphere-2023-1570
Preprint. Discussion started: 2 August 2023

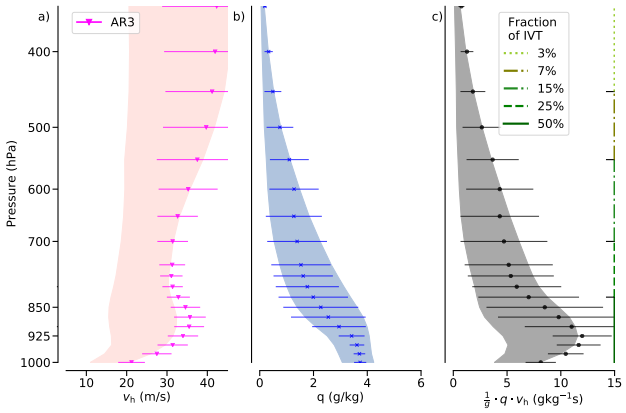

Figure 7. Vertical statistics of wind speed (a), specific humidity (b) and moisture transport (c) from the inflow cross-sections of the nine ARs analysed. Shaded areas represent the overall mean values ± the standard deviation. The error bars depict this distribution for the strongest AR (AR3). Vertical lines specify the cumulative contribution of moisture transport to IVT down to the given levels.

we quantify the relative standard deviations (s_q and s_v), normed by the mean, as a function of height (Fig. 8). In particular for the winds, the relative standard deviation remains rather consistent throughout the atmosphere and at a small magnitude (mean relative variability around 20 to 30 %), which is in line with the high but rather homogenous winds in the strong AR3 (Fig. 7). Besides a weak local maxima in the vicinity of the LLJ, the variability increases near the upper-level polar jet, however, with minor impact on the moisture transport (variability) due to dry airmasses.

The variability of moisture behaves differently. In the boundary layer, moisture variability is negligible, similar to wind ($s_q, s_v < 20\,\%$). Yet, the decline of mean moisture with height is opposed by the increase of its relative variability. Between 600 and 850 hPa, high moisture variability basically contributes to mean moisture transport variability, increasing half as high as its mean. The cross-sectoral moisture represents the more variable quantity in arctic ARs.

4.4 Coherence of moisture and wind

For the moisture transport, it is not only important whether moisture and wind anomalies are high separately (Sect. 4.3), but also how correlated they are and whether coherent pattern contribute significantly to AR-IVT (Q2). If they do, carefully collocated observations are essential to determine $TIVT$, otherwise independent estimates of mean moisture and wind are sufficient. The overall moisture transport $\overline{q \cdot v}$ basically is a combination of transport by the mean quantities $\overline{q}$ and $\overline{v}$ and their cross-sectoral variabilities, i.e spatial fluctuations q' and v', according to:

$$\overline{q \cdot v} = \overline{(\overline{q} + q')(\overline{v} + v')} = \overline{q} \cdot \overline{v} + \underbrace{\overline{q'\overline{v}}}_{=0} + \underbrace{\overline{\overline{q}v'}}_{=0} + \underbrace{\overline{q' \cdot v'}}_{\mathrm{cov}(q,v)} . \tag{6}$$

While the second and third summand equal zero, the last term represents the covariance cov() between q and v.

https://doi.org/10.5194/egusphere-2023-1570
Preprint. Discussion started: 2 August 2023

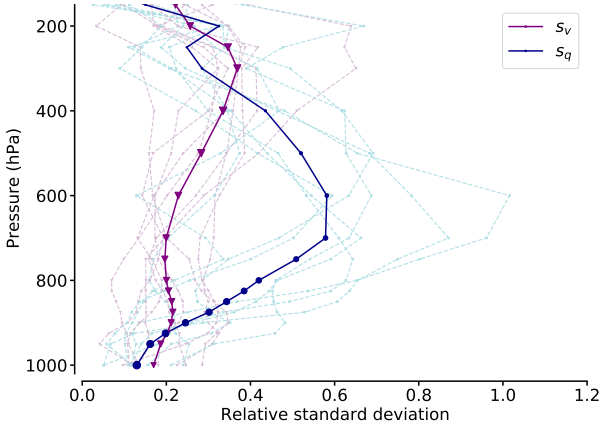

Figure 8. Vertical profile of relative standard deviation of wind (s_v) and moisture (s_q) for the AR cross-sections of each flight. The bold lines indicate the mean value over all ARs for both components. The sizes of the dots scale with the mean value at this height normed by the maximum mean value for the entire profile.

Using the relation between correlation coefficient r_{corr} and cov(), we obtain:

$$\text{cov}(q, v) = r_{\text{corr}}(q, v) \cdot \text{std}(q) \cdot \text{std(v)}, \tag{7}$$

and expanding by $\overline{q}$ and $\overline{v}$, we can reformulate Eq. 6 as:

$$\overline{q \cdot v} = \overline{q} \cdot \overline{v} \cdot (1 + \underbrace{r_{\text{corr}}(q, v) \cdot \underbrace{\frac{\text{std}(q)}{\overline{q}}}_{s_q} \cdot \underbrace{\frac{\text{std}(v)}{\overline{v}}}_{s_v}}_{cov_{\text{norm}}}). \tag{8}$$

The right summand in Eq. 8, the normalised covariance cov_{norm}, weights the coherent transport relative to the non-coherent. Using cov_{norm}, we find rather little coherence between moisture and wind in arctic AR cross-sections (Fig. 9). The magnitude of the contribution of moisture transport variability to the overall moisture transport is below $\pm 10\,\%$ for each height. Accordingly, the coherence is of minor influence for the entire IVT variability. Main reasons for the low contribution of coherent patterns are the relatively low standard deviations compared to their mean (see s_q and especially s_v). Even considerable correlation ($r_{\text{corr}} \geq 0.5$, Fig. 9) cannot generate relevant moisture transport contributions. Over the vertical extension, cov_{norm} mostly remains below 5 %. Even in moisture transport dominated levels (below 700 hPa), the cross-sections reveal a contribution of moisture transport variability to Eq. 8 in the range of 5 to 10 %. Only for some ARs, the strongest variability ($> \pm 10\,\%$) primarily occurs in higher levels above 500 hPa, where, in turn, moisture transport is weak (Fig. 7 and Fig. 9).

As correlation between moisture and wind r_{corr} shows a large spread between the single ARs (grey lines in Fig. 9), Figure 10 illustrate the spatial patterns of moisture and wind for our cross-sections. As already shown for the mean r_{corr}, the correlation between moisture and wind peaks in the LLJ height ($r_{\text{corr}} > 0.7$ for all ARs except for AR1, AR8, AR9). However, the variability of wind is small, as winds are almost constant along the entire cross-section ($> 25\,\text{ms}^{-1}$ especially in AR1 and AR3).

https://doi.org/10.5194/egusphere-2023-1570
Preprint. Discussion started: 2 August 2023

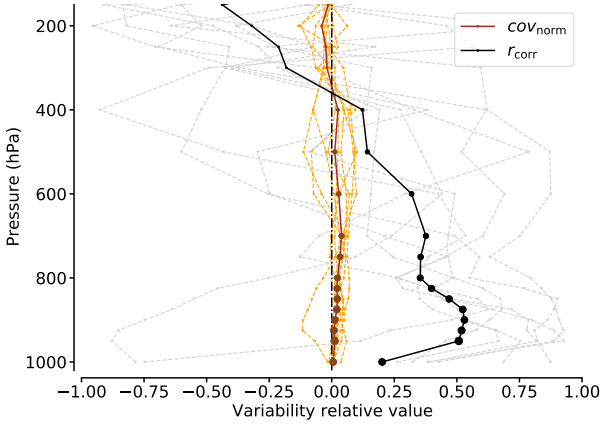

Figure 9. Vertical profile of AR moisture and wind normalised covariance (cov_{norm}) and their correlation r_{corr} along the cross-sections. The bold lines indicate the mean value over all AR for each of the components. The sizes of the dots scales with the mean moisture transport value at this height normed by the maximum mean value of the entire profile.

Here, it is the moisture variability steering the moisture transport variability. Such moisture variable ARs consist of an elevated moist layer only persisting in the AR core and surrounded by dry air.

The slanted structure of moisture transport in AR cross-sections (depicted in e.g. Ralph et al., 2004; Cordeira et al., 2013 Ralph et al., 2017) mostly reflects for AR5 where moisture and wind are most coherent. Residing in the warm conveyor belt, moist air masses lift over the cold-frontal sector. The downward intrusion of the upper-level jet on the eastern flank causes the slanted structure in the moisture transport. Other ARs exhibit less coherent pattern and wind and moisture do not necessarily align with each other. For example, AR9 indicates a clear displacement causing a negative cross-sectoral correlation.

We conclude that the mean moisture and wind account for 95 % of overall moisture transport in arctic ARs. Moisture and wind patterns are little coherent and show high inter-case variability. Strong ARs ($IVT \geq 400\,\text{kgm}^{-1}\text{s}^{-1}$) tend to feature strong, rather constant winds. Narrowed moisture columns here form the moisture transport variability. We recommend supplementary measurements of moisture to effectively increase the accuracy of AR moisture transport estimates. Incoherent cross-section patterns motivate investigating separate sectors along the AR front as they exhibit different processes (Cobb et al., 2021a). When moisture and wind regimes are independent, we expect cross-frontal differences in the divergence components of Eq. 4.

5 Moisture transport divergence from sondes

After assessing how sondes reproduce moisture transport variability (Sect. 4), we focus on IVT divergence. This section examines how the divergence of moisture transport is characterised along cross-sections of arctic ARs (Q3). We investigate whether high moisture advection (Eq. 4) occurs more frequently in strong moisture-dominated ARs and whether mass convergence dominates in windy AR corridors. Synthetic sondes illuminate how discrete soundings reflect such characteristics.

https://doi.org/10.5194/egusphere-2023-1570
Preprint. Discussion started: 2 August 2023

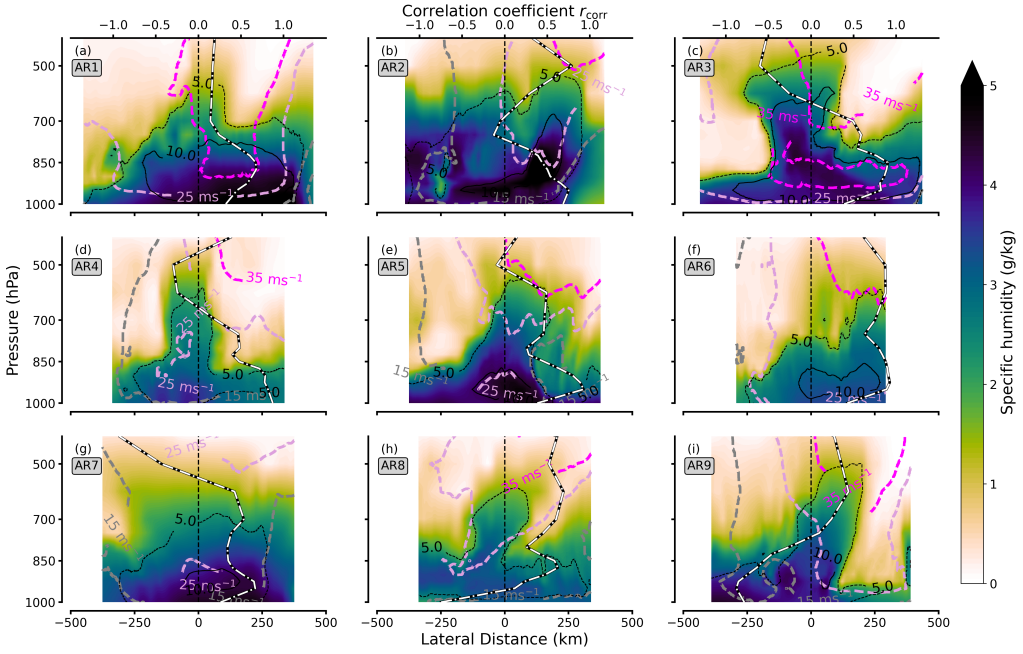

Figure 10. Cross-sections of AR inflow legs for moisture (color-coded contours), as well as wind contour lines for (pinkish) and moisture transport (both as contour lines). Shown moisture transport values have the unit $\mathrm{gkg^{-1}ms^{-1}}$. The black-white dashed vertical line represents the cross-sectoral mean of the correlation coefficient r_{corr} between moisture and wind for each pressure level.

5.1 Sectoral in- and outgoing moisture transport

In a first step, we depict the cross-sectoral IVT of the in- and outflow leg and their AR-$TIVT$ for all nine arctic ARs (Fig. 11). The leg comparison reveals a first simplified understanding of divergence. Idealising that no entrainment into the AR corridor (Sect. 5) takes place, we can contrast in- and outflow $TIVT$ in order to gain benchmarks whether convergence or divergence of internal moisture transport overall exists. Maximum IVT values vary between 200–650 $\mathrm{kg\,m^{-1}s^{-1}}$, whereby the outflow IVT generally exhibits a similiar intensity as the inflow leg. The strongest AR in terms of maximum IVT also has the highest total transport throughout both flight legs. $TIVT$ overall ranges from 100–300 $\cdot 10^6\,\mathrm{kg\,s^{-1}}$. Some arctic AR cross-sectoral $TIVT$ tends to decrease downstream. Higher IVT causing higher $TIVT$ in the inflow leg potentially suggests total convergence in the AR corridor. Still, we identify cases with little streamward tendencies of total moisture transport and others that even show divergence. This downstream difference of $TIVT$ is distributed unevenly over the cross-sectoral IVT.

Figure 11 separates the AR cross-sections in the three sectors (pre-frontal, core, post-frontal) as introduced in Sect. 3.3. Although the AR cores are roughly 200–300 km narrow (slim lines in Fig. 11), they provide more than half of AR-$TIVT$. Except for AR2 and AR7, weaker slopes of IVT are generally in the cold sector as opposed to the warm sector. The steep post-frontal IVT decline in AR2 and AR7 suggests different evolution processes associated with a high pressure ridge, favoured by anticyclonic rossby wave breaking (Zavadoff and Kirtman, 2018). While we mainly find IVT decreasing towards the outflow

https://doi.org/10.5194/egusphere-2023-1570
Preprint. Discussion started: 2 August 2023

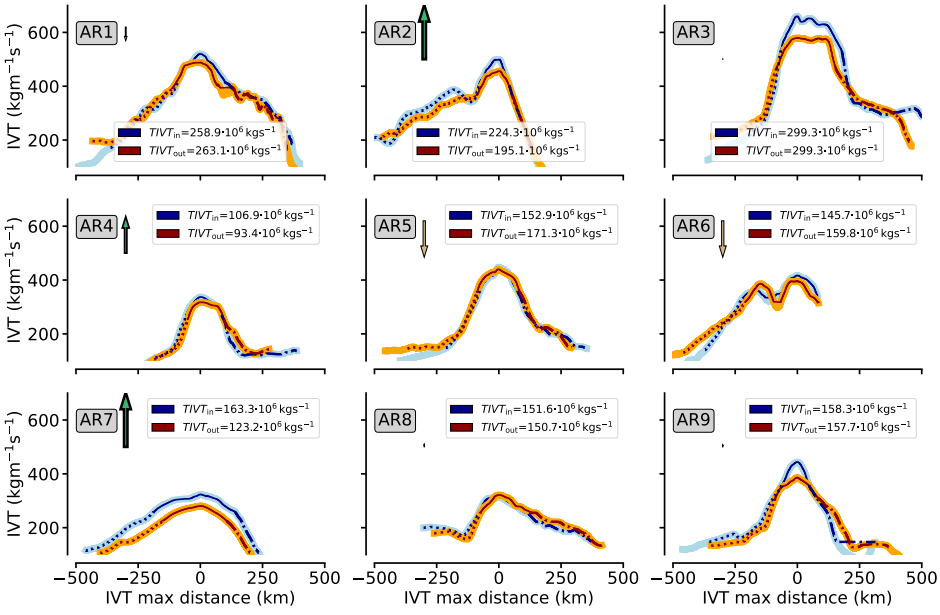

Figure 11. AR-IVT of inflow (outflow) section in blue (orange) for all nine corridors in the ARs. The domains of frontal specifc AR sectors are denoted by the line pattern changing. Dotted (dashed) lines represent the warm pre-frontal (cold post-frontal) sectors using the criteria mentioned in Sect. 3.2. Leg specific values for AR-$TIVT$ are specified in the legend. They purely include IVT internal of we declare as AR borders in Sect. 3.3 (dotted lines). Upward (downward) arrows roughly estimate corridor IVT convergence (divergence). Their length and width scales with the difference of $TIVT$ between both flight legs.

core, IVT occasionally intensifies in the two frontal sectors. They partially overcompensate the core leading to downstream net $TIVT$ gain. Yet, a $TIVT$-based interpretation of predominant moisture transport divergence underlies strong idealisation; Neither it considers moisture flow being not flight perpendicular, nor does it separate contributions of moisture advection and mass convergence. The regression approach is required to diagnose moisture transport divergence in each sector of arctic ARs.

5.2 Sonde-based divergence and its representativeness

This section specifies the regression-based (Sect. 3.2) IVT divergence (∇IVT) in arctic ARs for the frontal sectors (Sect. 3.3) using the decomposed terms, namely moisture advection ADV and mass convergence $CONV$ (Eq. 4). We compare our ∇IVT with that based on the mid-latitude study of Guan et al. (2020). The results we obtain from the continuous cross-sections interpolated from CARRA represent our idealised reference. For them and seven synthetic sondes per cross-section (as in Fig. 4), we apply the regression method to derive ADV and $CONV$. We build on the airborne study of Norris et al. (2020), investigating a mid-latitude AR event, and assess uncertainties of sonde-based determination of ∇IVT in arctic ARs.

For the intense AR3, Figure 12 delineates the divergence components specified for the frontal sectors. In the continuous AR representation, ADV and $CONV$ behave differently throughout the frontal cross-section, as stated in Guan et al.

https://doi.org/10.5194/egusphere-2023-1570
Preprint. Discussion started: 2 August 2023

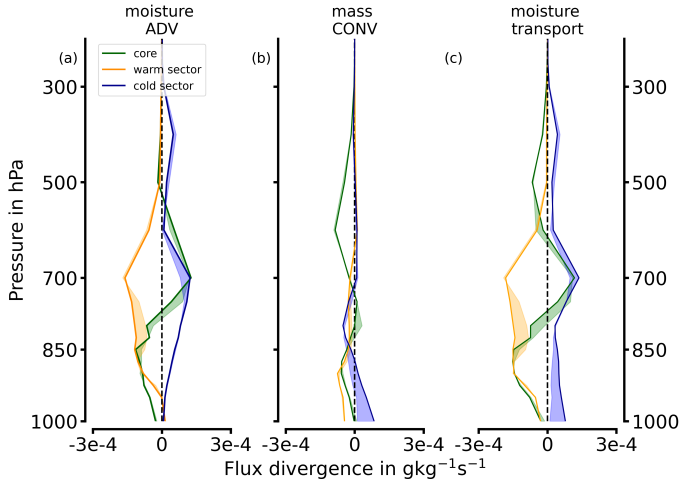

Figure 12. Vertical contributions from ADV (a) and $CONV$ (b) to the moisture transport divergence (c) for the frontal sectors in AR3. Bold lines represent sonde-based values whereas the filled areas denote the deviation to values based on continuous AR representation.

(2020) and Norris et al. (2020). While $CONV$ does not rise above $\pm 1 \cdot 10^{-4}\,\mathrm{g\,kg^{-1}s^{-1}}$ in the warm sector, ADV exceeds $\pm 2 \cdot 10^{-4}\,\mathrm{g\,kg^{-1}s^{-1}}$. The cold sector even shows dry advection ($ADV > 0$) in the lower atmosphere. The ADV dominance contradicts the case observed by Norris et al. (2020), where ADV was small compared to $CONV$. They, in turn, observed a more intense mid-latitude AR near its centre. Our corridors along the sea ice edge can be primarily attributed to the AR exit region as the centre is located southwards (see Fig. 2). For AR3, the moisture transport convergence (divergence) manifests in the warm (cold) sector when we integrate along the vertical axis (not shown). This is similar to what is found in mid-latitudes (Guan et al., 2020). In AR3, ADV and $CONV$ act on different vertical levels. Their maxima locate at the heights where also moisture and wind dominate, respectively (Fig. 10). In the warm sector, moisture advection increases above 850 hPa while mass converges closer to the surface and less intense. The core represents a transition zone with low-level moisture advection but signifcant drying in mid-levels (700 hPa). The LLJ characterises a weak mass convergence maximum ($\approx -0.75 \cdot 10^{-4}\,\mathrm{g\,kg^{-1}s^{-1}}$). The cold sector exhibits vertically consistent drying by advection (dominating) and mass divergence.

Three synthetic sondes in each frontal sector leg (located as in Fig. 4) generally reproduce the divergence characteristics of the continuous reference within each AR frontal sector. The highest deviations occur for the warm sector arising from moisture advection misrepresentation. Slight cross-sectoral displacements of the sonde positions emerge in changing divergence characteristics, but they do all maintain the principle vertical characteristics for each component and sector (Fig. 12). Setting our sonde results in context to the airborne study of Norris et al. (2020), we identify the strength of real dropsondes having a high vertical resolution that provides much more vertical variability. Thus, the lower divergence in Fig. 12 presumably does not only result from less intense divergence in arctic ARs compared to mid-latitude ARs, but is also due to the coarser vertical grid.

To quantify the contribution of moisture transport divergence (such as in Fig. 12) to the moisture budget (Eq. 2), its vertical integral ∇IVT is required (Eq. 4). For our ARs, we summarise their daily contribution to the moisture budget in mm d^{-1} (Fig.

https://doi.org/10.5194/egusphere-2023-1570
Preprint. Discussion started: 2 August 2023

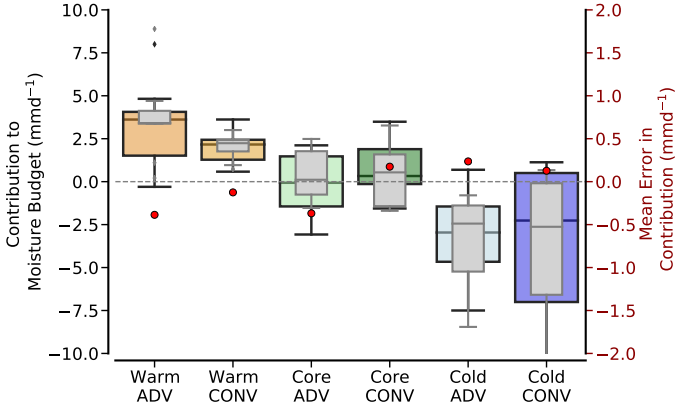

Figure 13. Box plot of moisture transport divergence contributions to daily moisture budget for all nine ARs. Values specify both components (ADV, $CONV$) for all frontal AR sectors. They compare the ideal AR representation (coloured box-whiskers) with the sonde-based values (grey box-whiskers). The boxes refer to the quartiles and horizontal lines inside specify the respective mean value.

13). The warm pre-frontal sector overall supplies moisture with advection being twice as dominant as convergence. In contrast, the post-frontal cold sector clearly constitutes a moisture sink. The strongest drying is found here from mass divergence. The post-frontal sector exhibits the highest inter-event variability. The core marks the transition zone with positive and negative contributions prevailing for both components. Mass convergence shows a slightly stronger, more robust positive tendency. We note that the range of absolute values from -6 mm d^{-1} to +4 mm d^{-1} is pretty small compared to Guan et al. (2020). In particular, the mass convergence is little compared to their mid-latitude cases (by a factor of 10). Hence, triggering of precipitation is presumably much less pronounced while moisture advection leads to an increase in the atmospheric moisture reservoir.

Applying three soundings per sector, the sondes replicate the cross-frontal divergence (grey whiskers in Fig. 13), i.e. the relatively weak mass convergence omnipresent for our arctic ARs. This contradicts Guan et al. (2020) who found dominating mass convergence in and ahead of the AR front. However, our values can not be intercompared naively. Besides our different AR regions (AR exit region at the sea ice edge that is more distant to the AR centre, Fig. 2), our investigated frontal sectors are larger than pixel-based values used in Guan et al. (2020). In turn, our horizontal resolution includes subscale variability.

Taking into account the observability of moisture transport divergence by discrete dropsondes, our configurations derive similar median values as the continuous AR representation. For our arctic AR composition, this confirms that three sondes per sector are basically capable to reproduce the general frontal structure of moisture transport divergence and its vertically integrated contribution to the moisture budget. However, as the percentiles between sondes and continuous representation deviate, the soundings can misinterpret the magnitude of the sector-specific divergence components considerably for the individual events. Since this deviation is unbiased though, the sonde mean errors remain below 0.5 mm d^{-1}. We remind that, while precedent moisture budget studies mostly refer to single time steps or at least conduct a time-to-space adjustment (Norris et al., 2020), we mimic the observations in the light of the flight duration. The airborne non-instantaneous perspective can cause differences in our understanding of the AR corridors as the AR evolves meanwhile.

https://doi.org/10.5194/egusphere-2023-1570
Preprint. Discussion started: 2 August 2023

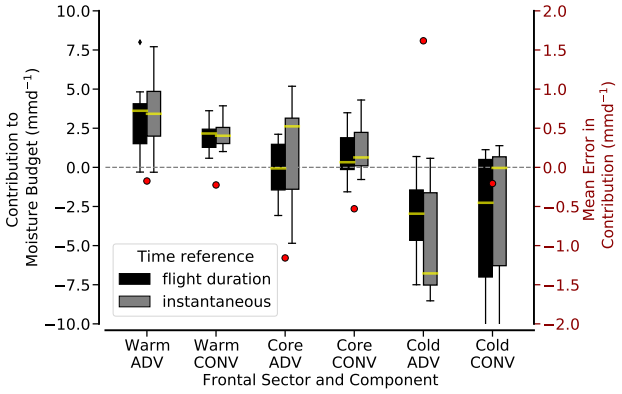

Figure 14. Comparison of divergence component contributions to daily moisture budget from the continuous AR representation referring either on the time-propagating flight values or when using the values for the centered hour. Values are given for each frontal sector. Black error bars are identical to the coloured boxes in Fig. 13. Grey values represent the centered hour based values.

6 Deterioration by non-instantaneous sounding

This section evaluates to what extent the discrete synthetic sondes reproduce IVT divergence in the light of temporal AR evolution during flight (Q4). We quantify the error in observed moisture transport arising from the flight duration of up to 3 h to overpass AR corridors (Sect. 3.1.1), and to consecutively observe the in- and outflow legs. Within the AR corridor, the temporal AR evolution may deteriorate the airborne interpretation of Eulerian IVT divergence. As instantaneous reference, we establish the collocated AR representation from CARRA at the flight-centered hour.

In a first step, we contrast the cross-frontal ∇IVT for both continuous temporal representations (non-instantaneous and instantaneous). On average for all cases, the frontal gradient of ∇IVT is well captured by the non-instantaneous representation (Fig. 14). However, we note that the mean error in divergence arising from the flight duration (red dots in Fig. 14) is more pronounced than the error by sonde-based undersampling (compare to Fig. 13). In some sectors, the mean error exceeds more than $1\,\mathrm{mm\,d^{-1}}$, whereas sonde undersampling (Fig. 13) only induces mean errors below $0.5\,\mathrm{mm\,d^{-1}}$. The temporal evolution of the AR throughout the flight can thus strongly deteriorate the divergence estimates for individual sectors.

Although both temporal representations identify moisture advection (ADV) as the dominating factor for moisture transport divergence, it is ADV in the core and post-frontal sector where we find the highest deviations ($\geq \pm 1\,\mathrm{mm\,d^{-1}}$) compared to the instantaneous snapshot (Fig. 14). The deviations show up in the mean, median and standard deviation. In the cold post-frontal sector (core), the mean error and median of ADV consistently reveal more drying (moistening). Non-instantaneous sampling in instationary ARs changes the derived moisture budget contribution by more than 10 %, especially for ADV in the cold-sector rising above 25 % (comparing mean errors on right axis to boxplot values in Fig. 14). When we consider non-instantaneous deteriorations for individual ARs, we find cases with ADV errors exceeding more than $8\,\mathrm{mm\,d^{-1}}$ (not shown). The median of $CONV$ is much less affected. Relatively, however, $CONV$ exhibits higher mean errors but they have less impact on the absolute moisture transport divergence.

https://doi.org/10.5194/egusphere-2023-1570
Preprint. Discussion started: 2 August 2023

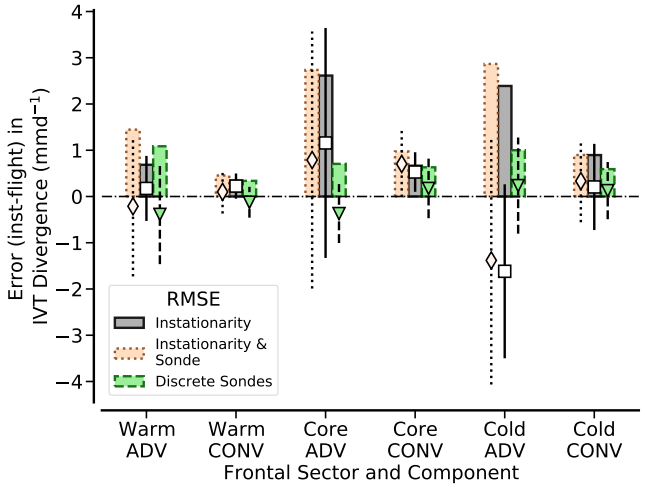

Figure 15. Total (orange) and individual errors only by discrete sondes (green) and only by instationarity (grey) for daily IVT divergence in each frontal sector and divergence component (Eq. 4). For all AR cross-sections, positive bars indicate the root-mean-square error (RMSE) while error markers and lines depict mean errors in combination with their standard deviations for the ARs.

The before-mentioned error tendencies result from the slanted movement of the AR, not necessarily aligned with moisture transport direction. In fact, all our ARs evolve more or less northeastwards, while our flight pattern is more zonally orientated, aiming for transport-orthogonal cross-sections. Since the winds exhibit less horizontal variability (Sect. 4.4), changes in mass convergence ($CONV$) which are lower than ADV remain less sensitive to non-instantaneous sampling and AR displacement. In-depth flight planning involving weather forecasts may help to adapt the flight pattern for AR evolution. Forecasts can estimate the mean propagation velocity and direction of the AR corridor center so that in- and outflow legs can be shifted.

Having purely referred to the continuous sampling of moisture transport before, we finally contrast the uncertainty arising from discrete spatial sampling by sondes and from non-instantaneous sampling in time. Using the root-mean-square error (RMSE), we compare the different samplings (continuous and discrete) in both time perspectives with our reference, the continuous and instantaneous representation. The subsampling errors are minor against the instationarity induced errors and cannot compensate the latter although they occasionally act in the opposite directions (Fig. 15). The non-instantaneous induced RMSEs are much higher (up to more than $2\,\mathrm{mm\,d^{-1}}$) than the ones originating from spatial undersampling. While the warm pre-frontal sector shows the highest positive moisture budget contributions regardless of the error criteria (Fig. 14), this sector does not have the highest RMSE for both error sources (Fig. 15). The largest errors occur in the core and post-frontal sector. Non-instantaneous sampling can misrepresent the divergence components by 50 % of the actual values (compare with Fig. 13).

Moisture advection (ADV) values react more sensitively than mass convergence ($CONV$) ones to airborne sampling. In contrast to sonde undersampling, instationarity-induced errors in ADV act in a more consistent direction (error bars in Fig. 15). Especially in the cold sector, AR instationarity mainly causes an airborne underestimation in dry advection. In the instantaneous reference, drier airmasses are already more embedded in the post-frontal inflow cross-section but differ less in the

https://doi.org/10.5194/egusphere-2023-1570
Preprint. Discussion started: 2 August 2023

outflow transect. This gradient overall reinforces dry advection. Consequently, we generally expect the strongest sonde-based misrepresentation in the cold post-frontal sector for such a zig-zag flight pattern.

Similar to the error magnitudes, the inter-case variability in divergence misrepresentation is much higher in ADV. The large inter-AR variability of the errors (Fig. 15) highlights that more cases should be considered to generalise the errors for arctic ARs. This includes differentiating ARs not only by their strength, but by their AR corridor type (entrance, centre, exit). If a zig-zag flight is more located in an intense AR centre, we expect the contribution of mass convergence and the errors due to the sounding intervals to increase so that $CONV$ becomes more comparable to Guan et al. (2020) and Norris et al. (2020). However, such AR conditions are rarely met close to the sea ice in spring (Fig. 2). The occurence of AR exit corridors over arctic sea ice is considerably higher. This underpins the usefullness of our benchmarks for dedicated arctic research flights.

7 Summary and conclusions

This observability study investigates to what extent sporadic airborne dropsondes can represent the Integrated Water Vapour Transport (IVT) variability and its divergence inside arctic Atmospheric Rivers (ARs). We elaborate on arctic AR conditions at the sea ice edge in Spring which have so far received less attention than mid-latitude ARs (e.g. Eiras-Barca et al., 2018; Ralph et al., 2019; Cobb et al., 2021a; Eiras-Barca et al., 2021). Since sophisticated airborne observations for arctic ARs do not yet exist, we make use of the high-resolution CARRA reanalysis. The AR representation in CARRA forms our idealisation of the reality (that outperforms the AR-IVT ERA5 variability) to estimate the background IVT variability in arctic ARs. In CARRA, we locate zig-zag flight patterns to cover the frontal sectors over the entire AR transect. The CARRA values are spatiotemporally interpolated onto the flight track. Single vertical profiles represent our synthetic dropsondes. The divergence is derived by regression methods (Stevens et al., 2019). We characterise uncertainties using dropsondes to monitor the AR moisture transport divergence. The synthetic sondes quantify the impacts resulting from discrete subsampling for IVT variability and their divergence representation. Second, sonde profiles along flight patterns are non-instantaneous. We thus elucidate how sonde-based IVT accuracy can be deteriorated by displacement and evolution of the AR over the flight duration.

Our investigation of AR moisture transport in CARRA marks a detailed analysis of arctic AR-IVT expanding on mid-latitude studies of AR moisture budget (Guan et al., 2020). Using finer reanalyses manifolds our understanding of arctic moisture transformation and will facilitate disentangling key processes of AR precipitation efficiency. Still, we are aware that our airborne emulation does not maintain all physical equilibria within the reanalysis. Considering corridors in nine arctic ARs in the vicinity of the sea ice edge, we rather intend to determine benchmarks of uncertainties in moisture transport divergence, steming from sonde undersampling and the flight duration. This synthetic assessment concludes the four pursued questions (Q1-Q4) as:

What is the maximum distance between sondes to determine the total moisture transport through AR corridors? (Q1)

- For the Total Integrated Water Vapour Transport ($TIVT$) of arctic AR cross-sections, sonde distances below 100 km have to be envisioned to certainly keep $TIVT$ errors below 10 %. In strong ARs with IVT exceeding 500 kg m^{-1}s^{-1}, too coarse IVT representation at the AR core leads to $TIVT$ underestimation. Gaussian fits help reproduce the cross-

https://doi.org/10.5194/egusphere-2023-1570
Preprint. Discussion started: 2 August 2023

sectoral IVT shape but are sensitive to how sondes estimate maximum IVT and its location. We suggest a minimum of five soundings per cross-section to derive $TIVT$ in both boundary legs as first estimate of IVT divergence appropriately.

How correlated are moisture and winds in arctic ARs and do coherent patterns contribute significantly to IVT? (Q2)

- The cross-sections do not universally indicate coherent moisture and wind patterns. Both variables can be poorly correlated due to spatial separation. Maximum contributions of moisture and wind to IVT and its lateral variability act on different vertical levels. Moisture variability remains relevant up to about 700 hPa, when the AR core implies elevated moist layers. Wind variability is more crucial below 850 hPa. While lateral moisture transport variability contributes less than 10 % to its mean, the relative variability of both quantities respectively is higher. In a relative sense, the variability of moisture dominates. For instance, our strongest AR characterises high moisture variability, whereas strong winds with little variability causes the transport of an overall rather small amount of moisture. We prioritise supplementary airborne measurements of moisture to better represent arctic AR-IVT variability. Unlike our northern cases, which are located more in the AR exit region, we expect wind variability to increase in corridors closer to the AR centre.

How does divergence of moisture transport characterise along the cross-section of arctic ARs? (Q3)

- By comparing in- and outflow IVT through the AR transects, we overall expect divergence in moisture transport. However, ARs exhibit frontal-specific characteristics in IVT divergence that have to be decomposed to moisture advection (ADV) and mass convergence ($CONV$), see Sect. 5. The pre-frontal AR sectors contribute to the moisture budget via both decomposits, whereas the post-frontal sectors overall indicate divergence. The core represents the zone of transition. Across the front, IVT divergence overall contributes to the moisture budget by up to +4 (pre-frontal convergence) to $-8\,\mathrm{mm\,d^{-1}}$ (post-frontal divergence). This is of half magnitude compared to the mid latitudes, but of high intensity for the Arctic. We generally find mass convergence dominating mainly below 850 hPa, while moisture advection governs above. Mass convergence is much less relevant than moisture advection.

To what extent can discrete non-instantaneous sondes reproduce IVT divergence in the light of AR evolution during flight? (Q4)

- Three sondes per frontal sector leg can reproduce the frontal gradient of divergence components with similar magnitudes of budget contribution (decline) in the pre-frontal (post-frontal) sector. The mean absolute error to the idealised AR representation extends to around $0.5\,\mathrm{mm\,d^{-1}}$. There is, in turn, high inter-case spread with positive and negative deviations. Sonde-based moisture advection turns out to be more sensitive. Nonetheless, the undersampling error becomes minor compared to the flight duration induced error. For the AR core and cold sector, the temporal AR evolution during the flight accounts for more than twice as high errors in ADV. Arising divergence errors can exceed 50 % of the actual values. In contrast to undersampling, errors induced by non-instantaneous sampling have a more consistent direction. For determined mass-convergence, errors remain small with the lowest differences occuring in the pre-frontal (warm) sector. We conclude that moisture advection on the arctic AR boundaries is both most contributing to the moisture trans-

https://doi.org/10.5194/egusphere-2023-1570
Preprint. Discussion started: 2 August 2023

port divergence and most sensitive to the airborne strategy as the ARs do not necessarily displace along the moisture transport direction.

Overall, we confirm the observability of moisture transport divergence in arctic AR corridors by releasing sondes in such dedicated flight patterns. A minimum of seven sondes per AR cross-section can prinicpally characterise the divergence under the given uncertainties of $\approx 10\,\%$. They determine divergence in a way that they cover cross-frontal gradients. The entire moisture transport divergence can be obtained with an uncertainty lower than 25 %. We emphasise the higher importance of supplementary measurements for moisture when faced with a limited amount of dropsondes, as moisture represents the more varying quantity in our AR corridors. Since our results mainly rely on corridors in the AR exit region, we strongly recommend an extension of our uncertainty assessment to other AR regions, and postulate the role of winds and mass convergence to increase in strong ARs moving more poleward. This emerges as an even more hot topic with respect to polar ARs tending to shift more northward and intensifying under climate change (O'Brien et al., 2022).

Our provided orders of magnitudes for IVT variability and divergence are representative for arctic ARs and quantify benchmarks in dropsonde-based derivation. Consistently mimicking the soundings is a fundamental stepstone to achieve an understanding of the uncertainties when such airborne tactics will actually be performed. For real sondes, we highlight the added value of the high vertical resolution. Sondes reveal more precise information of the vertical composition of ADV and $CONV$. We deduce that sonde undersampling matters and recommend a sequence of at least seven sondes per cross-section. Yet, notwithstanding that we could release a much higher number of sondes, it is the temporal AR evolution over flight duration that leads to higher deviations in divergence components rather than sonde undersampling. Thus, dedicated planning of such sonde-based observation purposes should not only involve dropsonde positioning but rather pursue minimising the flight duration. We postulate collocated flights where both cross-sections are sampled simultaneously by two aircraft as the optimum and still feasible strategy. The benchmarks are not only useful to improve flight strategies, but also indicate deviations in corresponding model-observation comparisons. Only when we illuminate the constraints of AR representation from both models and observations, we establish a framework from which airborne observations can support modellers in terms of resolution and complexity required for parametrizations of moisture transformation processes caused by IVT divergence in arctic ARs.

Code and data availability. The code created by HD that analyses the downloaded reanalyses and creates the figures can be accessed via github and is made available under: https://github.com/hdorff94/Synthetic_Airborne_Arctic_ARs. The reanalysis data from CARRA (Schyberg et al., 2021) and ERA5 (Hersbach et al., 2018) were accessed from the Copernicus Climate Change Service(C3S) Climate Data Store (CDS). The AR catalogue used to pre-identify AR events of interest (Guan, 2022) is provided by Bin Guan via https://ucla.box.com/ARcatalog.

https://doi.org/10.5194/egusphere-2023-1570
Preprint. Discussion started: 2 August 2023

Author contributions. HD, FA and HK were main initiators for the work in the scope of this manuscript. FA, HK and VS helped to conceptualise the manuscript. HD conducted the analysis presented and drafted the manuscript under scientific supervision of FA, HK and VS. All authors contributed to revising the manuscript.

Competing interests. The authors declare that they have no conflict of interest.

Acknowledgements. This study was supported by the Deutsche Forschungsgemeinschaft (DFG; German Research Foundation) under the HALO SPP 1294. We explicitly acknowledge the Copernicus Climate Change Service (C3S) Climate Data Store (CDS) for providing access to CARRA and ERA5 data. We thank Bin Guan for making the AR catalogue publically available via https://ucla.box.com/ARcatalog. Furthermore, we want to thank Melanie Lauer and Geet George for various helpful discussions. Henning Dorff is thankful to Jochem Marotzke and Dallas Murphy for providing fruitful comments on the writing style and structure of the manuscript. Thanks also go towards Norbert Noreiks for delivering sketches of the research aircraft.

https://doi.org/10.5194/egusphere-2023-1570
Preprint. Discussion started: 2 August 2023

References

Bengtsson, L., Andrae, U., Aspelien, T., Batrak, Y., Calvo, J., de Rooy, W., Gleeson, E., Hansen-Sass, B., Homleid, M., Hortal, M., Ivarsson, K.-I., Lenderink, G., Niemelä, S., Nielsen, K. P., Onvlee, J., Rontu, L., Samuelsson, P., Muñoz, D. S., Subias, A., Tijm, S., Toll, V., Yang, X., and Køltzow, M. Ø.: The HARMONIE–AROME Model Configuration in the ALADIN–HIRLAM NWP System, Monthly Weather Review, 145, 1919–1935, https://doi.org/10.1175/mwr-d-16-0417.1, 2017.

Bony, S. and Stevens, B.: Measuring Area-Averaged Vertical Motions with Dropsondes, Journal of the Atmospheric Sciences, 76, 767–783, https://doi.org/10.1175/jas-d-18-0141.1, 2019.

Cobb, A., Michaelis, A., Iacobellis, S., Ralph, F. M., and Monache, L. D.: Atmospheric River Sectors: Definition and Characteristics Observed Using Dropsondes from 2014–20 CalWater and AR Recon, Monthly Weather Review, 149, 623–644, https://doi.org/10.1175/mwr-d-20-0177.1, 2021a.

Cobb, A., Monache, L. D., Cannon, F., and Ralph, F. M.: Representation of Dropsonde-Observed Atmospheric River Conditions in Reanalyses, Geophysical Research Letters, 48, https://doi.org/10.1029/2021gl093357, 2021b.

Cobb, A., Ralph, F. M., Tallapragada, V., Wilson, A. M., Davis, C. A., Monache, L. D., Doyle, J. D., Pappenberger, F., Reynolds, C. A., Subramanian, A., Black, P. G., Cannon, F., Castellano, C., Cordeira, J. M., Haase, J. S., Hecht, C., Kawzenuk, B., Lavers, D. A., Murphy, M. J., Parrish, J., Rickert, R., Rutz, J. J., Torn, R., Wu, X., and Zheng, M.: Atmospheric River Reconnaissance 2021: A Review, Weather and Forecasting, https://doi.org/10.1175/waf-d-21-0164.1, 2022.

Cordeira, J. M., Ralph, F. M., and Moore, B. J.: The Development and Evolution of Two Atmospheric Rivers in Proximity to Western North Pacific Tropical Cyclones in October 2010, Monthly Weather Review, 141, 4234–4255, https://doi.org/10.1175/mwr-d-13-00019.1, 2013.

Demirdjian, R., Norris, J. R., Martin, A., and Ralph, F. M.: Dropsonde Observations of the Ageostrophy within the Pre-Cold-Frontal Low-Level Jet Associated with Atmospheric Rivers, Monthly Weather Review, 148, 1389–1406, https://doi.org/10.1175/mwr-d-19-0248.1, 2020.

Eiras-Barca, J., Ramos, A. M., Pinto, J. G., Trigo, R. M., Liberato, M. L. R., and Miguez-Macho, G.: The concurrence of atmospheric rivers and explosive cyclogenesis in the North Atlantic and North Pacific basins, Earth System Dynamics, 9, 91–102, https://doi.org/10.5194/esd-9-91-2018, 2018.

Eiras-Barca, J., Ramos, A. M., Algarra, I., Vázquez, M., Dominguez, F., Miguez-Macho, G., Nieto, R., Gimeno, L., Taboada, J., and Ralph, F. M.: European West Coast atmospheric rivers: A scale to characterize strength and impacts, Weather and Climate Extremes, 31, 100 305, https://doi.org/10.1016/j.wace.2021.100305, 2021.

Fearon, M. G., Doyle, J. D., Ryglicki, D. R., Finocchio, P. M., and Sprenger, M.: The Role of Cyclones in Moisture Transport into the Arctic, Geophysical Research Letters, 48, https://doi.org/10.1029/2020gl090353, 2021.

George, G., Stevens, B., Bony, S., Pincus, R., Fairall, C., Schulz, H., Kölling, T., Kalen, Q. T., Klingebiel, M., Konow, H., Lundry, A., Prange, M., and Radtke, J.: JOANNE: Joint dropsonde Observations of the Atmosphere in tropical North atlaNtic meso-scale Environments, Earth System Science Data, 13, 5253–5272, https://doi.org/10.5194/essd-13-5253-2021, 2021.

Gimeno, L., Nieto, R., VÃ¡zquez, M., and Lavers, D. A.: Atmospheric rivers: a mini-review, Frontiers in Earth Science 2, 2, https://doi.org/10.3389/feart.2014.00002, 2014.

Gorodetskaya, I. V., Tsukernik, M., Claes, K., Ralph, M. F., Neff, W. D., and Lipzig, N. P. M. V.: The role of atmospheric rivers in anomalous snow accumulation in East Antarctica, 41, 6199–6206, https://doi.org/10.1002/2014gl060881, 2014.

https://doi.org/10.5194/egusphere-2023-1570
Preprint. Discussion started: 2 August 2023

Graham, R. M., Cohen, L., Ritzhaupt, N., Segger, B., Graversen, R. G., Rinke, A., Walden, V. P., Granskog, M. A., and Hudson, S. R.: Evaluation of Six Atmospheric Reanalyses over Arctic Sea Ice from Winter to Early Summer, Journal of Climate, 32, 4121–4143, https://doi.org/10.1175/jcli-d-18-0643.1, 2019.

Guan, B.: Tracking Atmospheric Rivers Globally as Elongated Targets (tARget), Version 3 [Dataset], https://doi.org/10.25346/S6/YO15ON, 2022.

Guan, B. and Waliser, D. E.: Detection of atmospheric rivers: Evaluation and application of an algorithm for global studies, Journal of Geophysical Research: Atmospheres, 120, 12 514–12 535, https://doi.org/10.1002/2015jd024257, 2015.

Guan, B. and Waliser, D. E.: Atmospheric rivers in 20 year weather and climate simulations: A multimodel, global evaluation, Journal of Geophysical Research: Atmospheres, 122, 5556–5581, https://doi.org/10.1002/2016jd026174, 2017.

Guan, B., Waliser, D. E., and Ralph, F. M.: An Intercomparison between Reanalysis and Dropsonde Observations of the Total Water Vapor Transport in Individual Atmospheric Rivers, Journal of Hydrometeorology, 19, 321–337, https://doi.org/10.1175/jhm-d-17-0114.1, 2018.

Guan, B., Waliser, D. E., and Ralph, F. M.: A multimodel evaluation of the water vapor budget in atmospheric rivers, Annals of the New York Academy of Sciences, 1472, 139–154, https://doi.org/10.1111/nyas.14368, 2020.

Hersbach, H., Bell, B., Berrisford, P., Biavati, G., Horanyi, A., Sabater, J. M., Nicolas, J., Peubey, C., Radu, R., Rozum, I., Schepers, D., Simmons, A., Soci, C., Dee, D., and Thepaut, J.-N.: ERA5 hourly data on pressure levels from 1940 to present, Copernicus Climate Change Service (C3S) Climate Data Store (CDS) [data set] (accessed 22-Apr-2022), https://doi.org/10.24381/cds.bd0915c6, 2018.

Hersbach, H., Bell, B., Berrisford, P., Hirahara, S., Nicolas, J., Peubey, C., Radu, R., Schepers, D., Simmons, A., Soci, C., Abdalla, S., Abellan, X., Balsamo, G., Bechtold, P., Biavati, G., Bidlot, J., Bonavita, M., Chiara, G., Dahlgren, P., Dee, D., Diamantakis, M., Dragani, R., Flemming, J., Forbes, R., Fuentes, M., Geer, A., Haimberger, L., Healy, S., Hogan, R. J., Keeley, S., Laloyaux, P., Lopez, P., Lupu, C., Radnoti, G., Rosnay, P., Rozum, I., Vamborg, F., and Villaume, S.: The ERA5 global reanalysis, Quarterly Journal of the Royal Meteorological Society, 146, 1999–2049, https://doi.org/10.1002/qj.3803, 2020.

Kirbus, B., Tiedeck, S., Camplani, A., Chylik, J., Crewell, S., Dahlke, S., Ebell, K., Gorodetskaya, I., Griesche, H., Handorf, D., Höschel, I., Lauer, M., Neggers, R., Rückert, J., Shupe, M. D., Spreen, G., Walbröl, A., Wendisch, M., and Rinke, A.: Surface impacts and associated mechanisms of a moisture intrusion into the Arctic observed in mid-April 2020 during MOSAiC, Frontiers in Earth Science, 11, https://doi.org/10.3389/feart.2023.1147848, 2023.

Køltzow, M., Schyberg, H., Støylen, E., and Yang, X.: Value of the Copernicus Arctic Regional Reanalysis (CARRA) in representing near-surface temperature and wind speed in the north-east European Arctic, Polar Research, 41, https://doi.org/10.33265/polar.v41.8002, 2022.

Komatsu, K. K., Alexeev, V. A., Repina, I. A., and Tachibana, Y.: Poleward upgliding Siberian atmospheric rivers over sea ice heat up Arctic upper air, Scientific Reports, 8, https://doi.org/10.1038/s41598-018-21159-6, 2018.

Konow, H., Jacob, M., Ament, F., Crewell, S., Ewald, F., Hagen, M., Hirsch, L., Jansen, F., Mech, M., and Stevens, B.: A unified data set of airborne cloud remote sensing using the HALO Microwave Package (HAMP), Earth System Science Data, 11, 921–934, https://doi.org/10.5194/essd-11-921-2019, 2019.

Konow, H., Ewald, F., George, G., Jacob, M., Klingebiel, M., Kölling, T., Luebke, A. E., Mieslinger, T., Pörtge, V., Radtke, J., Schäfer, M., Schulz, H., Vogel, R., Wirth, M., Bony, S., Crewell, S., Ehrlich, A., Forster, L., Giez, A., Gödde, F., Groß, S., Gutleben, M., Hagen, M., Hirsch, L., Jansen, F., Lang, T., Mayer, B., Mech, M., Prange, M., Schnitt, S., Vial, J., Walbröl, A., Wendisch, M., Wolf, K., Zinner, T., Zöger, M., Ament, F., and Stevens, B.: EUREC4A's HALO, Earth System Science Data, 13, 5545–5563, https://doi.org/10.5194/essd-13-5545-2021, 2021.

https://doi.org/10.5194/egusphere-2023-1570
Preprint. Discussion started: 2 August 2023

Lavers, D. A., Pappenberger, F., Richardson, D. S., and Zsoter, E.: ECMWF Extreme Forecast Index for water vapor transport: A forecast tool for atmospheric rivers and extreme precipitation, Geophysical Research Letters, 43, https://doi.org/10.1002/2016gl071320, 2016.

Lenschow, D. H., Savic-Jovcic, V., and Stevens, B.: Divergence and Vorticity from Aircraft Air Motion Measurements, Journal of Atmospheric and Oceanic Technology, 24, 2062–2072, https://doi.org/10.1175/2007jtecha940.1, 2007.

Mattingly, K. S., Mote, T. L., and Fettweis, X.: Atmospheric River Impacts on Greenland Ice Sheet Surface Mass Balance, JGR Atmospheres, 123, 8538–8560, https://doi.org/10.1029/2018jd028714, 2018.

Mech, M., Orlandi, E., Crewell, S., Ament, F., Hirsch, L., Hagen, M., Peters, G., and Stevens, B.: HAMP – the microwave package on the High Altitude and LOng range research aircraft (HALO), Atmospheric Measurement Techniques, 7, 4539–4553, https://doi.org/10.5194/amt-7-4539-2014, 2014.

Nash, D., Waliser, D., Guan, B., Ye, H., and Ralph, F. M.: The Role of Atmospheric Rivers in Extratropical and Polar Hydroclimate, Journal of Geophysical Research: Atmospheres, 123, 6804–6821, https://doi.org/10.1029/2017jd028130, 2018.

Neff, W.: Atmospheric rivers melt Greenland, 8, 857–858, https://doi.org/10.1038/s41558-018-0297-4, 2018.

Norris, J. R., Ralph, F. M., Demirdjian, R., Cannon, F., Blomquist, B., Fairall, C. W., Spackman, J. R., Tanelli, S., and Waliser, D. E.: The Observed Water Vapor Budget in an Atmospheric River over the Northeast Pacific, Journal of Hydrometeorology, 21, 2655–2673, https://doi.org/10.1175/jhm-d-20-0048.1, 2020.

O'Brien, T. A., Wehner, M. F., Payne, A. E., Shields, C. A., Rutz, J. J., Leung, L.-R., Ralph, F. M., Collow, A., Gorodetskaya, I., Guan, B., Lora, J. M., McClenny, E., Nardi, K. M., Ramos, A. M., Tomé, R., Sarangi, C., Shearer, E. J., Ullrich, P. A., Zarzycki, C., Loring, B., Huang, H., Inda-Díaz, H. A., Rhoades, A. M., and Zhou, Y.: Increases in Future AR Count and Size: Overview of the ARTMIP Tier 2 CMIP5/6 Experiment, Journal of Geophysical Research: Atmospheres, 127, https://doi.org/10.1029/2021jd036013, 2022.

Papritz, L. and Dunn-Sigouin, E.: What Configuration of the Atmospheric Circulation Drives Extreme Net and Total Moisture Transport Into the Arctic, Geophysical Research Letters, 47, https://doi.org/10.1029/2020gl089769, 2020.

Papritz, L., Aemisegger, F., and Wernli, H.: Sources and Transport Pathways of Precipitating Waters in Cold-Season Deep North Atlantic Cyclones, Journal of the Atmospheric Sciences, 78, 3349–3368, https://doi.org/10.1175/jas-d-21-0105.1, 2021.

Ralph, F. M., Neiman, P. J., and Wick, G. A.: Satellite and CALJET Aircraft Observations of Atmospheric Rivers over the Eastern North Pacific Ocean during the Winter of 1997/98, Monthly Weather Review, 132, 1721–1745, https://doi.org/10.1175/1520-0493(2004)132<1721:sacaoo>2.0.co;2, 2004.

Ralph, F. M., Neiman, P. J., and Rotunno, R.: Dropsonde Observations in Low-Level Jets over the Northeastern Pacific Ocean from CALJET-1998 and PACJET-2001: Mean Vertical-Profile and Atmospheric-River Characteristics, 133, 889–910, https://doi.org/10.1175/mwr2896.1, 2005.

Ralph, F. M., Iacobellis, S. F., Neiman, P. J., Cordeira, J. M., Spackman, J. R., Waliser, D. E., Wick, G. A., White, A. B., and Fairall, C.: Dropsonde Observations of Total Integrated Water Vapor Transport within North Pacific Atmospheric Rivers, Journal of Hydrometeorology, 18, 2577–2596, https://doi.org/10.1175/jhm-d-17-0036.1, 2017.

Ralph, F. M., Rutz, J. J., Cordeira, J. M., Dettinger, M., Anderson, M., Reynolds, D., Schick, L. J., and Smallcomb, C.: A Scale to Characterize the Strength and Impacts of Atmospheric Rivers, Bulletin of the American Meteorological Society, 100, 269–289, https://doi.org/10.1175/bams-d-18-0023.1, 2019.

Schyberg, H., Yang, X., Koltzow, M., Amstrup, B., Bakketun, A., Bazile, E., Bojarova, J., Box, J. E., Dahlgren, P., Hagelin, S., Homleid, M., Horanyi, A., Hoyer, J., Johansson, A., Killie, M., Koernich, H., Moigne, P. L., Lindskog, M., Manninen, T., Englyst, P. N., Nielsen, K., Olsson, E., Palmason, B., Aros, C. P., Randriamampianina, R., Samuelsson, P., Stappers, R., Stoylen, E., Thorsteinsson, S., Valkonen,

https://doi.org/10.5194/egusphere-2023-1570
Preprint. Discussion started: 2 August 2023

T., and Wang, Z.: Arctic regional reanalysis on pressure levels from 1991 to present, Copernicus Climate Change Service (C3S) Climate Data Store(CDS) (accessed on 16-Jun-2022), https://doi.org/10.24381/CDS.E3C841AD, 2021.

Seager, R. and Henderson, N.: Diagnostic Computation of Moisture Budgets in the ERA-Interim Reanalysis with Reference to Analysis of CMIP-Archived Atmospheric Model Data, Journal of Climate, 26, 7876–7901, https://doi.org/10.1175/jcli-d-13-00018.1, 2013.

Shupe, M. D., Rex, M., Blomquist, B., Persson, P. O. G., Schmale, J., Uttal, T., Althausen, D., Angot, H., Archer, S., Bariteau, L., Beck, I., Bilberry, J., Bucci, S., Buck, C., Boyer, M., Brasseur, Z., Brooks, I. M., Calmer, R., Cassano, J., Castro, V., Chu, D., Costa, D., Cox, C. J., Creamean, J., Crewell, S., Dahlke, S., Damm, E., de Boer, G., Deckelmann, H., Dethloff, K., Dütsch, M., Ebell, K., Ehrlich, A., Ellis, J., Engelmann, R., Fong, A. A., Frey, M. M., Gallagher, M. R., Ganzeveld, L., Gradinger, R., Graeser, J., Greenamyer, V., Griesche, H., Griffiths, S., Hamilton, J., Heinemann, G., Helmig, D., Herber, A., Heuzé, C., Hofer, J., Houchens, T., Howard, D., Inoue, J., Jacobi, H.-W., Jaiser, R., Jokinen, T., Jourdan, O., Jozef, G., King, W., Kirchgaessner, A., Klingebiel, M., Krassovski, M., Krumpen, T., Lampert, A., Landing, W., Laurila, T., Lawrence, D., Lonardi, M., Loose, B., Lüpkes, C., Maahn, M., Macke, A., Maslowski, W., Marsay, C., Maturilli, M., Mech, M., Morris, S., Moser, M., Nicolaus, M., Ortega, P., Osborn, J., Pätzold, F., Perovich, D. K., Petäjä, T., Pilz, C., Pirazzini, R., Posman, K., Powers, H., Pratt, K. A., Preußer, A., Quéléver, L., Radenz, M., Rabe, B., Rinke, A., Sachs, T., Schulz, A., Siebert, H., Silva, T., Solomon, A., Sommerfeld, A., Spreen, G., Stephens, M., Stohl, A., Svensson, G., Uin, J., Viegas, J., Voigt, C., von der Gathen, P., Wehner, B., Welker, J. M., Wendisch, M., Werner, M., Xie, Z., and Yue, F.: Overview of the MOSAiC expedition: Atmosphere, Elementa: Science of the Anthropocene, 10, https://doi.org/10.1525/elementa.2021.00060, 2022.

Stevens, B., Ament, F., Bony, S., Crewell, S., Ewald, F., Gross, S., Hansen, A., Hirsch, L., Jacob, M., Kölling, T., Konow, H., Mayer, B., Wendisch, M., Wirth, M., Wolf, K., Bakan, S., Bauer-Pfundstein, M., Brueck, M., Delanoë, J., Ehrlich, A., Farrell, D., Forde, M., Gödde, F., Grob, H., Hagen, M., Jäkel, E., Jansen, F., Klepp, C., Klingebiel, M., Mech, M., Peters, G., Rapp, M., Wing, A. A., and Zinner, T.: A High-Altitude Long-Range Aircraft Configured as a Cloud Observatory: The NARVAL Expeditions, Bulletin of the American Meteorological Society, 100, 1061–1077, https://doi.org/10.1175/bams-d-18-0198.1, 2019.

Tan, Y., Yang, S., Zwiers, F., Wang, Z., and Sun, Q.: Moisture budget analysis of extreme precipitation associated with different types of atmospheric rivers over western North America, Climate Dynamics, 58, 793–809, https://doi.org/10.1007/s00382-021-05933-3, 2021.

Vázquez, M., Algarra, I., Eiras-Barca, J., Ramos, A. M., Nieto, R., and Gimeno, L.: Atmospheric Rivers over the Arctic: Lagrangian Characterisation of Their Moisture Sources, Water, 11, 41, https://doi.org/10.3390/w11010041, 2018.

Wong, S., Genio, A. D. D., Wang, T., Kahn, B. H., Fetzer, E. J., and L'Ecuyer, T. S.: Responses of Tropical Ocean Clouds and Precipitation to the Large-Scale Circulation: Atmospheric-Water-Budget-Related Phase Space and Dynamical Regimes, Journal of Climate, 29, 7127–7143, https://doi.org/10.1175/jcli-d-15-0712.1, 2016.

Woods, C. and Caballero, R.: The Role of Moist Intrusions in Winter Arctic Warming and Sea Ice Decline, Journal of Climate, 29, 4473–4485, https://doi.org/10.1175/jcli-d-15-0773.1, 2016.

You, C., Tjernström, M., and Devasthale, A.: Warm and moist air intrusions into the winter Arctic: a Lagrangian view on the near-surface energy budgets, Atmospheric Chemistry and Physics, 22, 8037–8057, https://doi.org/10.5194/acp-22-8037-2022, 2022.

Zavadoff, B. L. and Kirtman, B. P.: North Atlantic Summertime Anticyclonic Rossby Wave Breaking: Climatology, Impacts, and Connections to the Pacific Decadal Oscillation, Journal of Climate, 32, 485–500, https://doi.org/10.1175/jcli-d-18-0304.1, 2018.

Zhang, C., Tung, W.-W., and Cleveland, W. S.: Atlas of Arctic Atmospheric River Climatology Based on ERA5 and MERRA-2, https://doi.org/10.1002/essoar.10511981.1, 2022.

https://doi.org/10.5194/egusphere-2023-1570
Preprint. Discussion started: 2 August 2023

690 Zheng, M., Monache, L. D., Wu, X., Ralph, F. M., Cornuelle, B., Tallapragada, V., Haase, J. S., Wilson, A. M., Mazloff, M., Subramanian, A., and Cannon, F.: Data Gaps within Atmospheric Rivers over the Northeastern Pacific, Bulletin of the American Meteorological Society, 102, E492–E524, https://doi.org/10.1175/bams-d-19-0287.1, 2021.